

# The effects of aircraft on climate and pollution. Part I: Numerical methods for treating the subgrid evolution of discrete size- and composition-resolved contrails from all commercial flights worldwide

M.Z. Jacobson<sup>a,\*</sup>, J.T. Wilkerson<sup>a</sup>, A.D. Naiman<sup>b</sup>, S.K. Lele<sup>b</sup>

<sup>a</sup> Dept. of Civil and Environmental Engineering, Stanford University, Stanford, CA, USA

<sup>b</sup> Dept. of Aeronautics and Astronautics, Stanford University, Stanford, CA, USA

## ARTICLE INFO

### Article history:

Received 27 January 2011

Received in revised form 15 March 2011

Accepted 16 March 2011

Available online 22 March 2011

### Keywords:

Aerosol microphysical algorithms

Numerical methods

3-D computer models

Aerosol composition

Aerosol-cloud interactions

## ABSTRACT

This paper provides and evaluates mass conservative, positive-definite, unconditionally-stable, and non-iterative numerical techniques for simulating the evolution of discrete, size- and composition-resolved aerosol and contrail particles in individual aircraft exhaust plumes in a global or regional 3-D atmospheric model and coupling the subgrid exhaust plume information to the grid scale. Such treatment represents a new method of simulating the effects of aircraft on climate, contrails, and atmospheric composition. Microphysical processes solved within each plume include size-resolved coagulation among and between aerosol and contrail particles and their inclusions, aerosol-to-hydro-meteor particle ice and liquid nucleation, deposition/sublimation, and condensation/evaporation. Each plume has its own emission and supersaturation, and the spreading and shearing of each plume's cross-section are calculated as a function of time. Aerosol- and contrail-particle core compositions are tracked for each size and affect optical properties in each plume. When line contrails sublimate/evaporate, their size- and composition-resolved aerosol cores and water vapor are added to the grid scale where they affect large-scale clouds. Algorithm properties are analyzed, and the end-result model is evaluated against in situ and satellite data.

© 2011 Elsevier Inc. All rights reserved.

## 1. Introduction

This paper provides numerical techniques for simulating the evolution of aerosol and contrail particles with discrete size resolution within individual aircraft exhaust plumes in a global or regional atmospheric model and for coupling the subgrid exhaust plume information to the grid scale. The treatment represents a new method of simulating the effects of aircraft on climate, contrails, and atmospheric composition.

Previous global modeling studies of the effects of aircraft exhaust, while pioneering, have treated contrails at the grid scale rather than at the subgrid scale and as bulk parameters rather than with discrete size or composition resolution (e.g., [39,35,27,3,37]).

For this study, mass-conservative, unconditionally-stable, positive-definite, and noniterative numerical techniques are provided to simulate the discrete size- and composition-resolved microphysical evolution of aircraft exhaust at the subgrid scale (at their actual size). Among the new processes discussed are (1) segmentation of the flight-track and its corresponding size- and composition-resolved aerosol emissions for each individual flight into its own exhaust plume within each grid cell

\* Corresponding author.

E-mail address: [Jacobson@stanford.edu](mailto:Jacobson@stanford.edu) (M.Z. Jacobson).

of a 3-D model, (2) size- and composition-resolved coagulation among and between all such particles and their chemical inclusions, (3) the determination of a unique supersaturation for each exhaust plume based on emitted and ambient water vapor, aerosol particle size and composition, and temperature, (4) aerosol nucleation to ice or liquid contrail particles as a function of aerosol composition, size, and supersaturation, (5) ice deposition/sublimation and condensation/evaporation onto discrete size-resolved aerosol particles, (6) transition of the remnants of subgrid linear contrails to grid-scale cirrus and other clouds, and (7) radiative effects of subgrid linear contrails as a function of ice crystal size and composition and contrail plume shape. These methods are combined here with a previously method of calculating the spreading and shearing of individual aircraft line contrail cross sections over time as a function of grid-scale diffusion and wind shear [32].

The benefit of subgrid treatment of aircraft-related variables is that it removes the unrealistic assumptions that emissions are instantaneously mixed to the grid scale, that contrail size distributions and compositions from all aircraft in a grid cell are the same and merged upon emission to produce a grid-cell average, that supersaturations for contrail formation are the same for all aircraft in a grid cell, and that contrail widths are fixed. Instead, the new treatment allows for the unique microphysical and dynamical evolution of each aircraft exhaust plume until the material blends naturally into the grid-scale atmosphere. Treating aircraft exhaust at the subgrid scale does not eliminate parameterization; however, it reduces it, thereby reducing the number of tunable parameters while increasing the physical nature of the calculation. Because computer time of the global model used here increases by only 20–25% by treating over 31 million individual flights per year worldwide, there is no major computational limitation to using the techniques developed.

## 2. New treatment of aircraft emissions and contrail evolution

In this section, the new methods and equations for treating the microphysical evolution of subgrid aircraft exhaust plumes and merging them to the grid scale are discussed.

### 2.1. Partitioning flight-tracks into model exhaust plumes

The first step in treating each of millions of flights at the subgrid scale in a 3-D model is to convert each original flight track into its own aircraft plume within each model grid cell that the track passes through. The original flight tracks of each of the 31 million commercial flights worldwide used here were obtained for 2004 and 2006 from the Volpe National Transportation Systems Center, as described in detail in Wilkerson et al. [46].

Emission data from each flight in the original inventories were provided in segments with time increments between take-off and landing varying from seconds to tens of minutes. Since many flights take up to 15 h or more, all flights longer than 1 h are broken up here into hourly original segments, and same-GMT-hour original segments among all flights (short and long) are sequestered into hourly emission files, with flight track and emission data for each original segment of each flight during the hour stored in each file. Thus, the flight tracks for all flights in 2004 (2006) are divided into  $366 (365) \times 24$  hourly files with each file containing original segments of thousands of new or continuing flights during that hour.

Next, for each flight, all original segments from each hourly file are partitioned (if the segment length is longer than a grid cell) or summed (if multiple segments fit into a grid cell) into “new” model segments for each model grid cell each emission time step as follows. The original segments from each flight that fall within a model cell during a time step are summed to form one “new” segment in the cell for that flight. For example, in Fig. 1, the “new” segment in Cell 3 consists of a fraction of original segments B and D and all of original segment C. The “new” segments in Cells 4 and 2 consist of a fraction of Segment A and B, respectively. Emissions into each “new” segment are proportional to the fraction of the segment in the cell. Partitioning conserves mass along each flight's path.

On average, 3500 new flights commence worldwide each hour, but since many flights last several hours and some hours have more traffic than others, the number of new plus existing overall flights tracked worldwide in a given hour ranges from 5000–20,000. Since each flight has multiple segments (10–200 generally), the total number of segments treated simultaneously worldwide in a time step often exceeds 300,000. The time-dependent evolution of exhaust from each such segment is tracked over time in the model.

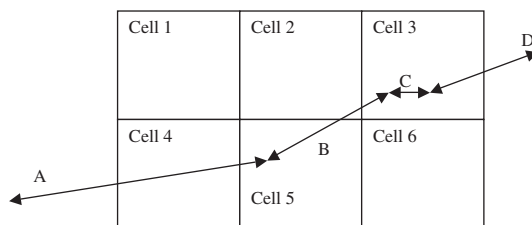


**Fig. 1.** Example of how flight segments cross grid cell boundaries. Segments A, B, C, and D are original segments. These are partitioned or aggregated into individual model grid cells 2, 3, 4, and 5 to form “new” segments, as described in the text.

## 2.2. Emissions into elliptical exhaust plumes

Emitted gases in each original segment of each flight include CO, CO<sub>2</sub>, H<sub>2</sub>O, speciated total hydrocarbons (THCs), NO<sub>x</sub>, and SO<sub>2</sub>. Emitted particle components include black carbon (BC), primary organic matter (POM), and sulfate [S (VI)]. In the present treatment, H<sub>2</sub>O, BC, POM, and S (VI) are emitted into each “new” subgrid segment plume within each grid cell each time step, whereas CO, CO<sub>2</sub>, SO<sub>2</sub>, NO<sub>x</sub>, and speciated THCs are emitted to the grid scale since these gases are assumed not to interact with line contrails much during the time scale of contrail evolution. For example, at  $T = 223$  K and  $p_a = 263$  hPa (10 km), the  $e$ -folding lifetimes of SO<sub>2</sub>, NO<sub>2</sub>, and toluene against OH oxidation at  $[OH] = 5 \times 10^5$  molec./cm<sup>3</sup> are  $\sim 14$ , 1.3, and 2.5 days, respectively, much longer than the few-hour lifetime of a line contrail. Since these gases are only slightly soluble and little liquid water exists in contrail particles at cruise altitude, such gases also do not dissolve readily in line contrail particles. Mixing gases instantly to a larger scale may affect ozone [24], but Vohralik et al. [44] found that this effect may be small for aircraft plume processing of global ozone. There is no reason the trace gases cannot be emitted into the plume as well in future work.

The total mass emissions of H<sub>2</sub>O, BC, POM, and S (VI) per unit time within each “new” segment is divided by the initial segment volume in the grid cell to obtain an initial mass concentration of each chemical in the “new” segment in the cell. The initial segment volume is the “new” segment length in the grid cell multiplied by an initial cross-sectional area of the plume. For example, the “new” segment length in Cell 3 of Fig. 1 is the sum of the lengths of Segments B, C, and D that fall within Cell 3. The initial cross-sectional area of each plume is assumed to be that of an ellipse ( $\pi ab$ ) with semimajor axis length  $a$  and semiminor axis length  $b$ . The ellipse area is held constant during each time step but  $a$  and  $b$  are each modeled to change at the beginning of each time step due to shear and diffusion using the subgrid plume model (SPM) analytical solution of Naiman et al. [32].

Because each time step for microphysical calculations in a subgrid plume is relatively long, the initial area of the ellipse needs to be greater than the area of the engine-out aerosol size distribution (taken at 2 s) and less than the area at the end of the time step. Based on large-eddy simulation (LES) results after 2 min [32], the initial values of  $a$  and  $b$  for microphysical calculations for the first time step are set to 90 m and 45 m, respectively. However, for the elliptical cross sectional area, predicted in time here with the SPM, to match those of LES results after 10 min and beyond under a variety of conditions, the initial values for dynamical calculations were determined from a best fit to be  $a = 155$  m and  $b = 135$  m. The reason the 2-min dimensions are not used to advance the SPM for the first time step, is that mean quantities of shear and diffusion, used to advance the SPM, do not capture the rapid changes in these quantities during the first few minutes of the LES; however, after 10 minutes, they do. The reason that the 2- rather than the 10-min dimensions are used for microphysical calculations initially is that the latter result in too much dilution of initial concentrations. Most coagulation and condensation/deposition in the plume occurs in the first two minutes, so such processes are artificially slowed if 10-min initial cross sections are used. In sum, two sets of initial cross sections are used, one for microphysical and one for dynamical (SPM) calculations. After the first time step, however, the elliptical cross section (thus plume volume and top-view area) is determined solely from the SPM calculation.

## 2.3. Creating discrete aerosol distributions from emitted aerosol mass

Within each subgrid aircraft exhaust plume, the model treats one aerosol-line-contrail (ALC) size distribution with any number of discrete size bins. Here, 16 discrete size bins between 0.8 nm and 8 mm in diameter are assumed. The broad size range allows aerosol and contrail particles to exist in the same size distribution. Total particle number concentration and the mole concentrations of individual components in each size bin are tracked over time within each plume (Table 2). Particles in the ALC size distribution include both aircraft-emitted and background particles. Both sources of aerosol particles are merged in an exhaust plume and can grow and dissipate within the plume.

To obtain an emission size distribution discretized into model size bins, the initial total mass concentration of each aerosol chemical [BC, POM, S (VI)] emitted into each “new” segment of each grid cell is first fit to a continuous trimodal log-normal emission distribution with the parameters in Table 2. Emissions are initialized with an engine-out size distribution based on data for plume ages  $< 2$  s [34] rather than for an aged distribution since the model calculates contrail evolution between the beginning and end of a time step. In Table 2, no BC exists in the smallest emission mode because BC is assumed to be an aggregate of spherules with the smallest spherule diameter of 14 nm [20]. Since BC is emitted within soot particles, which are BC aggregates coated by POM and S (VI), the smallest bin that BC can enter is set to 23.8 nm to ensure that if POM and S (VI) evaporate, the BC core will be no smaller than 14 nm. POM (which consists of unburned fuel oil) and S (VI) exist down to 0.8-nm diameter, the low diameter of the smallest bin. Thus, below 23.8 nm, emitted POM-S (VI) is internally mixed. Above this, emitted BC-POM-S (VI) is internally mixed. Liquid water and ice are not emitted but enter a size bin during contrail growth of water vapor, which is emitted and present in background air.

The continuous mass distribution for each chemical  $q$  is then discretized into a mass concentration ( $M_{q,i}$  g-particle/cm<sup>3</sup>-air) in each model size bin  $i$ . Mass concentrations are summed among all components in each size bin to obtain the total volume concentration (cm<sup>3</sup>-particle/cm<sup>3</sup>-air) of particles in the bin with

$$v_i = \sum_i v_{q,i} = \sum_i M_{q,i} / \rho_q = \sum_i m_q c_{q,i} / \rho_q \quad (1)$$

where  $v_{q,i}$  is the volume concentration and  $c_{q,i}$  is the mole concentration ( $\text{mol cm}^{-3}\text{-air}$ ) of component  $q$  [e.g., BC, POM, S (VI), water] in size bin  $i$ ,  $\rho_q$  is component density ( $\text{g/cm}^3$ ), and  $m_q$  is component molecular weight ( $\text{g/mol}$ ). Finally, the total number concentration (particles/ $\text{cm}^3\text{-air}$ ) in each size bin is calculated with

$$n_i = v_i/v_l \quad (2)$$

where  $v_l$  is the average single-particle volume ( $\text{cm}^3/\text{particle}$ ) in the bin. The particle number concentration and the mole concentrations of each component (Table 1) in each bin are then tracked over time in each plume.

#### 2.4. Aerosol- and contrail-particle coagulation

Due to high particle number concentrations, significant coagulation occurs in engine-out exhaust ( $<2$  s). However, temperatures are too high for water to condense or deposit, since a few to tens of seconds are needed to equilibrate exhaust temperatures with the ambient. As such, after emissions into a new aircraft plume, aerosol coagulation is solved first, followed by contrail-particle nucleation and growth. For aged aircraft plumes (those that persist after the first time step), the order of calculation is aerosol-contrail particle coagulation followed by contrail-particle growth or shrinkage. Section 3 reports the sensitivity of results to order of calculation. During all microphysical processes, particle number concentration and BC, POM, S (VI), and ice (or liquid) mole concentration in each size bin are tracked over time along with water vapor in each plume in each grid cell.

The integro-differential coagulation equation within each aircraft exhaust plume in each grid cell is solved over the aerosol-contrail size distribution with a semi-implicit solution [15]. This scheme is noniterative, positive-definite, unconditionally stable, and conservative of single-particle volume and volume concentration for all particle components and the total particle in each bin and among all bins. Number concentration converges to the exact solution upon an increase in resolution. The coagulation solution, in terms of the volume concentration ( $\text{cm}^3 \text{ cm}^{-3}\text{-air}$ ) of component  $q$  within particles in aerosol-contrail size bin  $k$  at time  $t$  after one time step  $h$  (s) is

**Table 1**

Subgrid aerosol-contrail and grid-scale aerosol and hydrometeor discrete size distributions treated in the model and the parameters present in each size bin of each size distribution.

Subgrid aerosol-contrail	Grid-Scale Aerosol Emitted Fossil-Fuel Soot (EFFS)	Grid-Scale Aerosol Internally Mixed (IM)	Grid-Scale Cloud/Precipitation Liquid	Grid-Scale Cloud/Precipitation Ice	Grid-Scale Cloud/Precipitation Graupel
Number	Number	Number	Number	Number	Number
BC	BC	BC	BC	BC	BC
POM	POM	POM	POM	POM	POM
S (VI)	SOM	SOM	SOM	SOM	SOM
H <sub>2</sub> O (aq)-c	H <sub>2</sub> O (aq)-h	H <sub>2</sub> O (aq)-h	H <sub>2</sub> O (aq)-h	H <sub>2</sub> O (aq)-h	H <sub>2</sub> O (aq)-h
H <sub>2</sub> O (s)	H <sub>2</sub> SO <sub>4</sub> (aq)	H <sub>2</sub> SO <sub>4</sub> (aq)	H <sub>2</sub> SO <sub>4</sub> (aq)	H <sub>2</sub> SO <sub>4</sub> (aq)	H <sub>2</sub> SO <sub>4</sub> (aq)
	HSO <sub>4</sub> <sup>-</sup>	HSO <sub>4</sub> <sup>-</sup>	HSO <sub>4</sub> <sup>-</sup>	HSO <sub>4</sub> <sup>-</sup>	HSO <sub>4</sub> <sup>-</sup>
	SO <sub>4</sub> <sup>2-</sup>	SO <sub>4</sub> <sup>2-</sup>	SO <sub>4</sub> <sup>2-</sup>	SO <sub>4</sub> <sup>2-</sup>	SO <sub>4</sub> <sup>2-</sup>
	NO <sub>3</sub> <sup>-</sup>	NO <sub>3</sub> <sup>-</sup>	NO <sub>3</sub> <sup>-</sup>	NO <sub>3</sub> <sup>-</sup>	NO <sub>3</sub> <sup>-</sup>
	Cl <sup>-</sup>	Cl <sup>-</sup>	Cl <sup>-</sup>	Cl <sup>-</sup>	Cl <sup>-</sup>
	H <sup>+</sup>	H <sup>+</sup>	H <sup>+</sup>	H <sup>+</sup>	H <sup>+</sup>
	NH <sub>4</sub> <sup>+</sup>	NH <sub>4</sub> <sup>+</sup>	NH <sub>4</sub> <sup>+</sup>	NH <sub>4</sub> <sup>+</sup>	NH <sub>4</sub> <sup>+</sup>
	NH <sub>4</sub> NO <sub>3</sub> (s)	NH <sub>4</sub> NO <sub>3</sub> (s)	NH <sub>4</sub> NO <sub>3</sub> (s)	NH <sub>4</sub> NO <sub>3</sub> (s)	NH <sub>4</sub> NO <sub>3</sub> (s)
	(NH <sub>4</sub> ) <sub>2</sub> SO <sub>4</sub> (s)	(NH <sub>4</sub> ) <sub>2</sub> SO <sub>4</sub> (s)	(NH <sub>4</sub> ) <sub>2</sub> SO <sub>4</sub> (s)	(NH <sub>4</sub> ) <sub>2</sub> SO <sub>4</sub> (s)	(NH <sub>4</sub> ) <sub>2</sub> SO <sub>4</sub> (s)
		Na <sup>+</sup> (K, Mg, Ca)	Na <sup>+</sup> (K, Mg, Ca)	Na <sup>+</sup> (K, Mg, Ca)	Na <sup>+</sup> (K, Mg, Ca)
		Soil dust	Soil dust	Soil dust	Soil dust
		Poll/spores/bact	Poll/spores/bact	Poll/spores/bact	Poll/spores/bact
			H <sub>2</sub> O (aq)-c	H <sub>2</sub> O (s)	H <sub>2</sub> O (s)

The contrail distribution within each subgrid contrail plume contained 16 size bins, the grid-scale aerosol distributions contained 14 size bins each, and the grid-scale hydrometeor distributions contained 30 size bins each. The components within each size bin of each size distribution were internally mixed in the bin but externally mixed from other bins and other distributions. Number is particle number concentration. All other variables are tracked in units of mole concentration (moles per cubic centimeter of air). POM is primary organic matter; SOM is secondary organic matter. H<sub>2</sub>O (aq)-h is liquid water hydrated to dissolved ions and undissociated molecules in solution. H<sub>2</sub>O (aq)-c is water that condensed to form liquid hydrometeors, and S(VI) = H<sub>2</sub>SO<sub>4</sub>(aq) + HSO<sub>4</sub><sup>-</sup> + SO<sub>4</sub><sup>2-</sup>. Condensed and hydrated water existed in the same particles so that, if condensed water evaporated, the core material, including its hydrated water, remained. H<sub>2</sub>O (s) was either water that froze or deposited from the gas phase as ice. The emitted species in the fossil-fuel soot distribution included BC, POM, H<sub>2</sub>SO<sub>4</sub>(aq), HSO<sub>4</sub><sup>-</sup>, and SO<sub>4</sub><sup>2-</sup>. The remaining species formed by gas-to-particle conversion or crystallization. Sea spray, soildust, biomass burning, biofuel burning, and other particles were emitted into the internally-mixed distribution. Emitted species in sea spray included H<sub>2</sub>O, Na<sup>+</sup>, K<sup>+</sup>, Mg<sup>2+</sup>, Ca<sup>2+</sup>, Cl<sup>-</sup>, NO<sub>3</sub><sup>-</sup>, H<sub>2</sub>SO<sub>4</sub>(aq), HSO<sub>4</sub><sup>-</sup>, and SO<sub>4</sub><sup>2-</sup>. Those in biomass burning included the same plus BC and POM. In both cases, K<sup>+</sup>, Mg<sup>2+</sup>, and Ca<sup>2+</sup> were treated as equivalent Na<sup>+</sup>. Soildust was generic. Homogeneously nucleated species (H<sub>2</sub>O, H<sub>2</sub>SO<sub>4</sub>(aq), HSO<sub>4</sub><sup>-</sup>, SO<sub>4</sub><sup>2-</sup>, and NH<sub>4</sub><sup>+</sup>) entered the internally-mixed distribution. Condensing gases on all distributions included H<sub>2</sub>SO<sub>4</sub> and SOM. Dissolving gases in all distributions included HNO<sub>3</sub>, HCl, and NH<sub>3</sub>. The liquid water content and H<sup>+</sup> in each bin were determined as a function of the relative humidity and ion composition from equilibrium calculations. All distributions were affected by self-coagulation loss to larger sizes and heterocoagulation loss to other distributions (except the graupel distribution, which had no heterocoagulation loss).

$$v_{q,k,t} = \frac{v_{q,k,t-h} + h \sum_{j=1}^k \left( \sum_{i=1}^{k-1} f_{i,j,k} \beta_{i,j} v_{q,i,t} n_{j,t-h} \right)}{1 + h \sum_{j=1}^{N_B} [(1 - f_{k,j,k}) \beta_{k,j} n_{j,t-h}]} \quad (3)$$

where  $\beta$  is the coagulation kernel (rate coefficient,  $\text{cm}^3 \text{ particle}^{-1} \text{ s}^{-1}$ ) between two particles in size bins  $i$  and  $j$ ,  $N_B$  is the number of discrete size bins, and

$$f_{i,j,k} = \begin{cases} \left( \frac{v_{k+1} - V_{ij}}{v_{k+1} - v_k} \right) \frac{v_k}{V_{ij}} & v_k \leq V_{ij} < v_{k+1} \quad k < N_B \\ 1 - f_{i,j,k-1} & v_{k-1} \leq V_{ij} < v_k \quad k > 1 \\ 1 & V_{ij} > v_k \quad k = N_B \\ 0 & \text{all other cases} \end{cases} \quad (4)$$

is the volume fraction of a coagulated pair  $i, j$ , with volume single-particle volume  $V_{ij} = v_i + v_j$ , partitioned into bin  $k$ . This intermediate particle has volume between those of two model bins,  $k$  and  $k + 1$ , and needs to be partitioned between the two.

The total coagulation kernel ( $\beta_{i,j}$ ,  $\text{cm}^3 \text{ particle}^{-1} \text{ s}^{-1}$ ) is the product of a coalescence efficiency and a collision kernel ( $\text{cm}^3 \text{ particle}^{-1} \text{ s}^{-1}$ ). Coalescence efficiencies are from Pruppacher and Klett [36, Eq. 14–28] for large particle radius 100–500  $\mu\text{m}$  and for small-to-large particle radius ratio 0.5–0.95; from Low and List [26] for other cases with small and large particle radii  $> 30 \mu\text{m}$ ; and from Beard and Ochs [2] for all other sizes. The collision kernel for the aerosol-contrail distribution combines kernels for Brownian motion, diffusion enhancement, van der Waal's forces, viscous forces, fractal geometry, gravitational settling, turbulent shear, and turbulent inertial motion [17].

Eq. (3) is solved in the order  $k = 1, \dots, N_B$ . No production occurs into the first bin,  $k = 1$ , since  $k - 1 = 0$  for the first bin in the numerator of Eq. (3). Thus, all necessary  $v_{q,i,t}$  terms are known when each  $v_{q,k,t}$  is calculated. Once the equation is solved,  $v_{k,t}$  ( $\text{cm}^3 \text{ cm}^{-3}\text{-air}$ ) and  $n_{k,t}$  (particles  $\text{cm}^{-3}$ ) are calculated from Eqs. (1) and (2), respectively, and new component mole concentrations ( $\text{mol cm}^{-3}\text{-air}$ ) are  $c_{q,k} = v_{q,k} \rho_q / m_q$ .

## 2.5. Determining a unique supersaturation in each plume

In each new plume, aerosol-aerosol coagulation is solved first, followed by nucleation, then growth. In each aged plume, aerosol-aerosol and aerosol-contrail coagulation are solved first and simultaneously (since aerosols exist in the same distribution as contrail particles), followed by growth/shrinkage. In both cases, each of the multiple plumes in each grid cell has a unique supersaturation calculated from the water vapor emitted by the aircraft added to the background water vapor and from the background temperature.

Ambient temperature is used to calculate supersaturation since exhaust temperatures equilibrate with ambient temperatures within a few to tens of seconds, but the time step for contrail physical processes is tens of minutes, so the effective temperature over a time step is effectively the ambient temperature. The total water vapor mole concentration ( $\text{mol-H}_2\text{O cm}^{-3}\text{-air}$ ) in each exhaust plume,  $C_v$ , is obtained by summing the grid-scale water vapor with the water vapor emitted by the aircraft into the plume, modified over time by plume expansion and condensation/deposition. As such, each subgrid plume has its own water vapor mole concentration and supersaturation, and both vary over time as the plume ages. If the grid-scale relative humidity is high, this results in a high grid-scale water vapor content added to the contrail plume.

## 2.6. Contrail particle nucleation

Line contrail particles form only if they nucleate during the first time step after emissions. In subsequent steps, the exhaust plume is too dilute for contrail formation. If a contrail does not form during the first step or if an aged contrail dissipates, the plume aerosol material and vapor are added to the grid scale, where they can affect cirrus or other clouds.

Ice contrails in the model can nucleate below and liquid contrails can nucleate above 258.15 K. This threshold is selected since above 258.15 K, soot does not activate as an ice nucleus when the air is supersaturated with respect to ice but does activate as a liquid nucleus when the air is supersaturated with respect to liquid water [4,36, p. 321]. Because liquid contrails are rare and ice contrails rarely form above 233.15 K, a threshold other than 258.15 K has little practical impact.

Aircraft soot particles activate to contrail ice crystals below 258.15 K by homogeneous freezing of liquid water on soot or heterogeneous ice nucleation of soot prior to water saturation. Soot particles can activate to liquid drops above 258.15 K upon reaching water saturation, although such activation generally occurs only in fogs near the surface. In all cases, a threshold water vapor mole concentration ( $C_{v,nuc}$ ,  $\text{mol cm}^{-3}\text{-air}$ ) above which activation of soot can occur, is first determined from

$$C_{v,nuc} = \begin{cases} \min[S_{230} C_{v,is}, C_{v,ls}] & T \geq 230 \text{ K} \\ [S_{185} + \frac{T-185}{230-185} (S_{230} - S_{185})] C_{v,is} & 230 > T \geq 185 \text{ K} \\ S_{185} C_{v,is} & T < 185 \text{ K} \end{cases} \quad (5)$$

where  $C_{v,is}$  and  $C_{v,ls}$  are the saturation mole concentrations ( $\text{mol cm}^{-3}\text{-air}$ ) of ice and liquid water, respectively, over a flat, dilute ice or liquid surface at a given temperature,  $T$  (K) is air temperature, and  $S_{185}$  and  $S_{230}$  are the saturation ratios over ice at 185 K and 230 K for which ice nucleates on contrail soot particles, based on laboratory data. Activation occurs when the

**Table 2**

Lognormal parameters and mass fractions of emitted material for three contrail emission modes.

	Mode 1	Mode 2	Mode 3
Geometric mean number diameter (nm)	5 <sup>a</sup>	34 <sup>a</sup>	150 <sup>a</sup>
Geometric standard deviation	1.37 <sup>b</sup>	1.55 <sup>a</sup>	1.65 <sup>a</sup>
Mass fraction of BC in mode	0 <sup>c</sup>	0.85 <sup>a</sup>	0.15 <sup>a</sup>
Mass fraction of POM in mode	0.07 <sup>d</sup>	0.85 <sup>d</sup>	0.08 <sup>d</sup>
Mass fraction of S (VI) in mode	0.07 <sup>d</sup>	0.85 <sup>d</sup>	0.08 <sup>d</sup>

Mass and number from each mode were distributed into a discrete aerosol-contrail size distribution for each chemical. <sup>a</sup> Petzold et al. [34], <sup>b</sup> Zhu et al. [49]; <sup>c</sup> BC emissions could not occur in mode 1 since the smallest spherule of a BC agglomerate is larger than this mode (see text). <sup>d</sup> POM and S (VI) fractions were similar to BC fractions, except that POM and S (IV) could be emitted into the smallest mode as they are volatile. The emission size distribution of surface combustion particles is given in [20]. The size distributions of sea spray and soil dust versus wind speed are given in Chapter 14 of Jacobson [17].

ambient water vapor mole concentration ( $C_v$ , mol cm<sup>-3</sup>-air) in a subgrid plume exceeds  $C_{v,nuc}$  (thus, if  $C_v > C_{v,nuc}$ ).  $C_v$  varies for each plume, as described in Section 2.5.

Eq. (5) suggests that, at  $T > 230$  K, soot can activate to ice (if  $T < 258.15$  K) either due to heterogeneous nucleation (if  $C_{v,ls} > C_v > S_{230}C_{v,ls}$ ) or homogeneous freezing (if  $S_{230}C_{v,ls} > C_v > C_{v,ls}$ ). Below 230 K, soot activation is assumed to be due to heterogeneous nucleation simply because, for  $T < 230$  K,  $C_{v,nuc} < C_{v,ls}$ .

Few data on saturation ratios for heterogeneous nucleation of ice on soot are available. Mohler et al. [31] measured  $S_{185} = 1.5$  and  $S_{230} = 1.3$  for soot particles coated by sulfate. Kanji and Abbott [22] measured  $S_{185} = 1.3$  and  $S_{230} = 1.1$  for pure (uncoated) soot particles. Based on a comparison of modeled contrail cloud fraction with satellite-derived data at high resolution over the US for separate months,  $S_{185} = 1.35$  and  $S_{230} = 1.15$  (which assumes only some initial soot coating by sulfate) give a much better comparison with data than  $S_{185} = 1.5$  and  $S_{230} = 1.3$ , which result in contrail cloud fractions that are too low.

## 2.7. Contrail growth

When new ice or liquid contrail particles form in a plume or when such particles persist from the previous time step, deposition/sublimation or condensation/evaporation equations are solved simultaneously between the plume's water vapor and all size bins of the aerosol-contrail size distribution. The numerical scheme conserves mass between the vapor and all size bins and is positive-definite, unconditionally-stable, and non-iterative.

For growth of liquid contrail particles (e.g.,  $T > 258.15$  K) the  $i = 1 \dots N_B$  ( $N_B$  = number of size bins) water condensation/evaporation equations and the corresponding gas conservation equation for the aerosol-contrail size distribution in each subgrid plume are

$$\frac{dc_{l,i,t}}{dt} = k_{l,i,t-h}(C_{v,t} - S'_{l,i,t-h}C_{v,ls,t-h}) \quad i = 1 \dots N_B \quad (6)$$

$$\frac{dC_{v,t}}{dt} = - \sum_{i=1}^{N_B} k_{l,i,t-h}(C_{v,t} - S'_{l,i,t-h}C_{v,ls,t-h}) \quad (7)$$

where  $t$  is current time (s),  $h$  is the time step (s),  $t-h$  is one time step back (s),  $c_{l,i,t}$  is the liquid water concentration (mol cm<sup>-3</sup>-air) within contrail particles of size  $i$ ,  $C_{v,t}$  is the contrail-plume water vapor concentration (mol cm<sup>-3</sup>-air) (the sum of ambient and aircraft-emitted water vapor)  $k_{l,i,t-h}$  is the transfer rate of vapor to liquid water surfaces (s<sup>-1</sup>),  $S'_{l,i,t-h}$  is the saturation ratio at equilibrium over liquid water drops, and  $C_{v,ls,t-h}$  is the initial water vapor saturation concentration over a flat, dilute liquid water surface (mol cm<sup>-3</sup>-air). Of these parameter,  $c_{l,i,t}$  and  $C_{v,t}$  are unknown over a time step and are solved, whereas the remaining parameters are held constant.

When new ice contrail particles nucleate ( $T \leq 258.15$  K) or ice contrail particles pre-exist, the analogous ice deposition/sublimation equations for each plume are

$$\frac{dc_{l,i,t}}{dt} = k_{l,i,t-h}(C_{v,t} - S'_{l,i,t-h}C_{v,ls,t-h}) \quad i = 1 \dots N_B \quad (8)$$

$$\frac{dC_{v,t}}{dt} = - \sum_{i=1}^{N_B} k_{l,i,t-h}(C_{v,t} - S'_{l,i,t-h}C_{v,ls,t-h}) \quad (9)$$

where  $c_{l,i,t}$  is the ice concentration (mol cm<sup>-3</sup>-air) within contrail particles of size  $i$ ,  $k_{l,i,t-h}$  is the transfer rate of vapor to ice surfaces (s<sup>-1</sup>),  $S'_{l,i,t-h}$  is the saturation ratio at equilibrium over ice, and  $C_{v,ls,t-h}$  is the water vapor saturation mole concentration over a flat, dilute ice surface (mol cm<sup>-3</sup>-air). Although ice crystals cannot nucleate until a vapor threshold is reached (Eq. (5)), once they do nucleate, the saturation vapor pressure used is that of ice without the threshold (but multiplied by the saturation ratio at equilibrium) since ice nucleation on a surface coats the surface, changing the vapor pressure to that of pure ice.



The saturation ratio at equilibrium over liquid drops accounts for Raoult's law and the Kelvin effect. The expression used is

$$S'_{L,i,t-h} \approx \frac{C_{L,i,t-h}}{C_{L,i,t-h} + f_s c_{POM,i,t-h} + 3c_{S(VI),i,t-h}} \exp\left(\frac{2\sigma_{L,i,t-h} m_w}{r_i R^* T \rho_L}\right) \quad (10)$$

where the exponential term is the Kelvin effect, which increases the saturation concentration over a curved relative to a flat surface, and the prefactor is Raoult's law, which decreases the saturation concentration over a concentrated drop relative to a dilute drop. Soluble components of aircraft exhaust include a portion of POM and S (VI). The parameters  $C_L$ ,  $c_{POM}$ , and  $c_{S(VI)}$  are the mol cm<sup>-3</sup>-air of liquid water, total POM, and S (VI), respectively, in a size bin, and  $f_s$  is the mole fraction of POM that is soluble, assumed to be 0.4, as aircraft POM contains from 20% (at low thrust) to 50–90% (high thrust) insoluble lubricating oil. Most of the rest is unburned hydrocarbons (HCs), some soluble and the rest, insoluble [45]. The prefactor (3) in front of  $c_{S(VI)}$  is the assumed number of moles of anions plus cations that S (VI) dissociates into.

In the Kelvin-effect term of Eq. (10),  $m_w$  is molecular weight of water (g mol<sup>-1</sup>),  $r_i$  is drop radius (cm),  $R^*$  is the gas constant ( $8.3145 \times 10^7$  g cm<sup>2</sup> s<sup>-2</sup> mol<sup>-1</sup> K<sup>-1</sup>),  $T$  is absolute temperature (K),  $\rho_L$  is liquid water density (g cm<sup>-3</sup>), and

$$\sigma_{L,i,t-h} = \sigma_{L,i,t-h,dilute} + \Delta\sigma_{L,i,t-h,wsoc} + \Delta\sigma_{L,i,t-h,inorg} \quad (11)$$

is the surface tension (g s<sup>-2</sup>) of a liquid particle solution, where  $\sigma_{L,i,t-h,dilute} = 76.1 - 0.155(T - 273.15)$  is the surface tension of pure liquid water [36], and

$$\Delta\sigma_{L,i,t-h,wsoc} = -0.0187T \ln\left(1 + 628.14 \frac{f_s c_{POM-i,t-h}}{C_{L,i,t-h} m_w} 1000 \frac{\text{g}}{\text{kg}}\right) \quad (12)$$

$$\Delta\sigma_{L,i,t-h,inorg} = +1.7 \frac{C_{S(VI),i,t-h}}{C_{L,i,t-h} m_w} 1000 \frac{\text{g}}{\text{kg}} \quad (13)$$

are the surface tension changes upon the addition of water-soluble organic carbon [8] and inorganic solutes [36], respectively.

In the case of ice, the saturation ratio at equilibrium is the Kelvin-effect term,

$$S'_{I,i,t-h} \approx \exp\left(\frac{2\sigma_{I,i,t-h} m_w}{r_i R^* T \rho_I}\right) \quad (14)$$

where  $\rho_I$  is the temperature-dependent mass density of ice (g cm<sup>-3</sup>) [36], and  $\sigma_{I,i,t-h} = 104.0 - 0.05(T - 273.15)$  is the surface tension (g s<sup>-2</sup>) of ice [36].

The transfer rate between water vapor and liquid drops is

$$k_{L,i,t-h} = \frac{n_{i,t-h} 4\pi r_i D_v \omega_{v,i,t-h} F_{v,L,i,t-h}}{\frac{D_v \omega_{v,i,t-h} F_{v,L,i,t-h} S'_{L,i,t-h} C_{v,L,i,t-h}}{\kappa_m \omega_{h,i,t-h} F_{h,L,i,t-h}} \left(\frac{L_e m_w}{T}\right) \left(\frac{L_e m_w}{R^* T} - 1\right) + 1} \quad (15)$$

where  $n_{i,t-h}$  is the number concentration of pre-existing or newly-activated contrail particles of size  $i$  (particles cm<sup>-3</sup>-air),  $D_v$  is the diffusion coefficient of water vapor in air (cm<sup>2</sup> s<sup>-1</sup>) [e.g., [17, Eq. 8.14]],  $\omega_{v,i,t-h}$  and  $\omega_{h,i,t-h}$  are dimensionless corrections for water vapor and energy, respectively, that account for collision geometry and sticking probability [*ibid.*, Eqs. 16.19, 16.27],  $F_{v,L,i,t-h}$  and  $F_{h,L,i,t-h}$  are dimensionless vapor and energy ventilation coefficients [*ibid.*, Eqs. 16.24, 16.31],  $L_e$  is the latent heat of evaporation (J g<sup>-1</sup>),  $\kappa_m$  is the thermal conductivity of moist air (J cm<sup>-1</sup> s<sup>-1</sup> K<sup>-1</sup>),  $T$  is temperature (K), and  $R^*$  is the gas constant (8.3145 J mole<sup>-1</sup> K<sup>-1</sup>). The parameters  $\omega_{v,i,t-h}$  and  $\omega_{h,i,t-h}$  require a mass accommodation (sticking) coefficient for water vapor on liquid water [set to 1.0, [47]] and a thermal accommodation coefficient [set to 0.96, [36]], respectively.

The number concentration of particles on which growth can possibly occur in a size bin in a given contrail plume is either the number concentration of freshly-emitted aerosol particles (for new plumes) or of pre-existing aerosol or contrail particles (for aged plumes) in the bin. For liquid contrails, the Köhler equation is used to determine the critical radius above which water vapor can grow onto particles in the size distribution. The critical radius and critical saturation ratio are  $r^* \approx \sqrt{3y/x}$  and  $S^* \approx 1 + \sqrt{4x^3/(27y)}$ , respectively, where  $x = 2\sigma_{L,i,t-h} m_w / (R^* T \rho_L)$  and  $y = 3m_w(f_s c_{POM,i,t-h} + 3c_{S(VI),i,t-h}) / (4\pi n_{i,t-h} \rho_L)$ . When  $r_i < r^*$  and  $S'_{L,i} < S^*$  or when  $r_i \geq r^*$  and  $C_v < S'_{L,i} C_{v,L}$ , existing liquid particles can evaporate in the size bin; otherwise, particles can grow. Whether the particles actually grow depend on the solution to the coupled gas-hydrometeor mass transfer equations, discussed shortly.

The mass transfer rate between water vapor and ice crystals is

$$k_{I,i,t-h} = \frac{n_{i,t-h} 4\pi \chi_i D_v \omega_{v,i,t-h} F_{v,I,i,t-h}}{\frac{D_v \omega_{v,i,t-h} F_{v,I,i,t-h} S'_{I,i,t-h} C_{v,I,i,t-h}}{\kappa_m \omega_{h,i,t-h} F_{h,I,i,t-h}} \left(\frac{L_s m_w}{T}\right) \left(\frac{L_s m_w}{R^* T} - 1\right) + 1} \quad (16)$$

where  $\chi_i$  is the crystal electric capacitance (cm),  $L_s$  is the latent heat of sublimation (J g<sup>-1</sup>),  $\omega_{v,i,t-h}$  and  $\omega_{h,i,t-h}$  are as in Eq. (15), except they use water vapor and thermal sticking coefficients for ice rather than liquid water, and  $F_{v,I,i,t-h}$  and  $F_{h,I,i,t-h}$  are dimensionless ventilation coefficients for vapor and energy over ice [17, Eq. 16.78]. Ice crystal habit, including the lengths of the major and minor semiaxes, is calculated as a function of temperature with data from Hindman and Johnson [13] from 273.15–243.15 K. These data indicate hexagonal plates at the lowest temperature. Goodman et al. [11] found that young

contrail ice crystals at 212 K were predominantly hexagonal plates, thus, we extended the shape parameters down to lower temperature. Capacitances as a function of major and minor semi-axes lengths were calculated with equations from Snow [42]. The water vapor sticking coefficient on ice is assumed to be 0.3, in the range 0.1–0.5 from Lin et al. [25]. The ice thermal sticking coefficient is assumed to be that of liquid water.

The number concentration of nucleated ice contrail particles at the beginning of a time step in a size bin of a plume equals zero for freshly-emitted soot if  $C_v \leq C_{v,nuc}$  in the plume; equals the number concentration of freshly-emitted soot if  $C_v > C_{v,nuc}$ ; or equals the number concentration of contrail particles already present for pre-existing contrail plumes, regardless of  $C_v$ . Pre-existing plume ice crystals can grow or evaporate when  $C_v \leq C_{v,nuc}$  since, once ice nucleates on soot, the criteria for growth/evaporation depends on whether Eq. (8) is positive or negative rather than on whether  $C_v > C_{v,nuc}$ . However, new particles can grow only if  $C_v > C_{v,nuc}$  and Eq. (8) is positive in the bin.

The solution to growth is an extension of the *Analytical Predictor of Condensation* (APC) scheme [15]. Below, the solution for liquid drops is given. The solution for ice crystals is analogous. Integrating Eqs. (6) and (7) for one size bin  $i$  in a single contrail plume over a time step  $h$  gives the final mole concentration of liquid water in the bin of the plume as

$$C_{L,i,t} = C_{L,i,t-h} + h k_{L,i,t-h} (C_{v,t} - S'_{L,i,t-h} C_{v,Ls,t-h}) \quad (17)$$

where the final gas mole concentration in the plume,  $C_{v,t}$ , is currently unknown. Final particle and gas concentrations are constrained by the gas-particle mass-balance equation,

$$C_{v,t} + \sum_{i=1}^{N_B} C_{L,i,t} = C_{v,t-h} + \sum_{i=1}^{N_B} C_{L,i,t-h} \quad (18)$$

Substituting Eq. (18) into Eq. (17) and solving for  $C_{v,t}$  gives a generalized solution for simultaneous condensation/evaporation within the plume,

$$C_{v,t} = \text{MIN} \left( \frac{C_{v,t-h} + h \sum_{i=1}^{N_B} k_{L,i,t-h} S'_{L,i,t-h} C_{v,Ls,t-h}}{1 + h \sum_{i=1}^{N_B} k_{L,i,t-h}}, C_{tot} \right) \quad (19)$$

The limit on Eq. (19) is placed since the explicit numerator can result in gas concentrations in excess of the maximum gas in the system. The equation cannot fall below zero.  $C_{v,t}$  is substituted back into Eq. (17) to give the final hydrometeor concentration in each bin. Since Eq. (17) can give negative or above-maximum concentrations, another limit is set after Eq. (19) is substituted back into it for all bins,

$$C_{L,i,t} = \begin{cases} C_{L,i,t-h} + \frac{C_{L,i,t} - C_{L,i,t-h}}{\sum_{j=1}^{N_B} \text{MAX}(C_{L,j,t} - C_{L,j,t-h}, 0)} \left[ C_{v,t-h} - C_{v,t} + \sum_{j=1}^{N_B} \text{MAX}(C_{L,j,t-h} - \text{MAX}(C_{L,j,t}, 0), 0) \right] & C_{L,i,t} > C_{L,i,t-h} \\ \text{MAX}(C_{L,i,t}, 0) & C_{L,i,t} \leq C_{L,i,t-h} \end{cases} \quad (20)$$

Finally, for cases where the above limits are invoked, the final gas concentration is recalculated as  $C_{v,t} = C_{v,t-h} + \sum_{j=1}^{N_B} (C_{L,j,t-h} - C_{L,j,t})$ . For all but a few conditions, this gives the exact result as Eq. (19). Under all conditions, the solution is exactly mass conserving between the gas and size-resolved hydrometeors, noniterative, and positive-definite.

## 2.8. Partitioning from a moving to fixed grid

Upon condensation or ice deposition, each subgrid contrail size distribution contains grown contrail particles and interstitial aerosol particles. The growth calculation assumes particles grow or shrink to their exact size regardless of bin boundaries (moving bin method). For coagulation, solved at the beginning of the next time step, it is useful to use fixed (stationary) size bins. As such, particles and their components are re-binned following growth to fixed bins in a number- and volume-conserving manner. The total-particle volume concentration ( $\text{mol cm}^{-3}\text{-air}$ ) in original moving bin  $i$  is re-binned between two adjacent fixed bins,  $k$  and  $k+1$  with  $v_k = f_{v,i,k} v_i$  and  $v_{k+1} = (1 - f_{v,i,k}) v_i$ , where

$$f_{v,i,k} = \left( \frac{v_{k+1} - v_i}{v_{k+1} - v_k} \right) \frac{v_k}{v_i} \quad (21)$$

is the volume fraction of particles from moving bin  $i$  partitioning to fixed bin  $k$ , and  $v$  is single-particle volume ( $\text{cm}^3 \text{ particle}^{-1}$ ). Individual components are similarly partitioned. The number concentration in fixed bin  $k$  is then  $n_{k,t} = v_{k,t}/v_k$ . This method conserves number and volume although it is somewhat numerically diffusive.

## 2.9. Line contrail shearing and spreading

After each operator-split time step of coagulation, growth/shrinkage, and rebinning within each line contrail plume in each grid cell, the dimensions  $a$  and  $b$  of the elliptical cross section of each plume are advanced with analytical solutions from the SPM over the same time step. The solution accounts for shearing and spreading of a cross-sectional ellipse as a function of grid-scale horizontal and vertical wind shear and diffusion [32]. Thus, plume volume, which is the product of



its cross-sectional area (which varies) and length (which stays constant), changes over time. Changes in plume volume change the concentration of each aerosol-contrail component and water vapor within each plume.

When liquid or ice water in a subgrid line contrail plume decreases below a threshold of  $10 \mu\text{g-water}/\text{m}^3$ , all of the plume's remaining material (water vapor, BC, POM, and S (VI) – Table 1) is added to the grid scale. At the grid scale, any number of discrete aerosol size distributions, size bins per distribution, and components per size bin can be treated. For the present application, two aerosol distributions, each with 14 size bins (2 nm–50  $\mu\text{m}$  diameter), are assumed. In each size bin of each aerosol distribution, particle number concentration and component mole concentrations are tracked (Table 1). The two aerosol distributions include an emitted fossil-fuel soot (EFFS) and an internally-mixed (IM) distribution. EFFS sources include vehicles, power plants, industry, ships, and aircraft. IM sources include the ocean (sea spray, bacteria), soils (dust, bacteria), volcanos, vegetation (pollen, spores), biofuel burning, biomass burning and coagulation from the EFFS distribution. Components within each size bin of each aerosol distribution are internally mixed in the bin but externally mixed from other bins and distributions. When line contrail particles dissipate, their remnant aerosol components are added to the EFFS size distribution. Since all latent heat released to the air during contrail formation is re-captured by water vapor during contrail sublimation/evaporation, there is no need to adjust the grid-scale temperature when exhaust plume material is added back to the grid scale.

## 2.10. Impacts of linear contrail remnants on other clouds

Once at the grid scale, linear contrail remnants (water vapor, aerosol particles, and trace gases, the last of which are emitted directly to the grid scale) can immediately affect or induce stratiform or cumulus clouds. The model treats grid-scale stratus clouds and multiple subgrid cumulus clouds in each column. For global simulations, stratus and cumulus thermodynamics are constrained by the quasi-equilibrium assumption; but all cloud microphysical processes are time-dependent, explicit, and size- and composition-resolved [16,17,19,21].

For stratiform and cumuliform clouds, the model treats three hydrometeor size distributions (liquid, ice, and graupel), each with 30 size bins (0.5  $\mu\text{m}$ –8 mm diameter) and multiple chemical components per bin (Table 1). Chemical inclusions within a hydrometeor particle are either aerosol components that the hydrometeor particle nucleates on or coagulates with or gases that dissolve in the particles and change phase. Remnant aerosol particles from line contrail can similarly serve as nuclei on which cumulus or stratiform cloud particles can grow on or coagulate with. As such, remnants of contrails feed back to other clouds, just as other aerosol particles do, through the first and second indirect effects and the cloud absorption effect. More details on aerosol particles feedbacks to cumulus and stratiform clouds in the model are given in Jacobson [19].

## 2.11. Radiative treatment of line contrails

Line contrails and the clouds they modify affect radiative heating and photolysis in the model. Spectral absorption optical depths, scattering optical depths, and asymmetry parameters for each subgrid aerosol-contrail size distribution are determined by multiplying aerosol-contrail number concentration in each size bin by single-particle cross-sectional area and single-particle absorption, scattering, and forward scattering efficiencies, respectively. Efficiencies for contrail ice crystals are calculated by assuming that all BC in a contrail particle is aggregated into a core surrounded by a shell, then applying Mie theory. As the model treats absorption by BC inclusions within contrail particles and BC-containing aerosol particles between contrail particles, it treats the radiative as well as microphysical (indirect) effects of aerosols on contrails.

When subgrid contrails exist, individual contrail cloud fractions are determined from contrail-plume top-view areas, which are calculated analytically Eq. [23 of 32]. The contrail cloud fraction in a column ( $c_{f,col}$ ) is then determined assuming random overlap among all individual contrails within each layer and among all column layers with

$$c_{f,col} = 1 - \prod_{i,k} (1 - c_{f,i,k}) \quad (22)$$

where  $c_{f,i,k}$  (e.g., [6]) is the cloud fraction of contrail  $i$  in layer  $k$ . Next, grid-scale column cloud fraction is determined by assuming random overlap among all subgrid contrails, subgrid cumulus clouds, and grid-scale stratiform clouds in the column (similar to Eq. (22)). Finally, radiative transfer is solved separately over cloudy and clear portions of each column, and the results are weighted by clear and cloudy-sky fractions. The radiative code and optical treatment of subgrid cumulus clouds and grid scale stratus clouds and aerosol particles are detailed in Jacobson [19].

## 2.12. Simplifications of the current approach

The approach described here contains some simplifying assumptions, such as ignoring line-contrail particle advection and sedimentation between grid cells. However, such simplifications are limited only to line contrails and not their remnants, which are advected and sediment once released to the grid scale. As such, contrail remnants from one grid cell can affect or induce cirrus and other clouds in adjacent grid cells.

Omitting line contrail sedimentation may have limited impacts in a global model. Ice crystals in contrails generally have an effective diameter <5  $\mu\text{m}$  (e.g., [11]), and 5  $\mu\text{m}$  particles require >10 days, much longer than maximum contrail lifetimes, to fall 1 km. Some line contrail particles grow to 30  $\mu\text{m}$ , but even these require >9 h to fall 1 km and are small in number.

Line contrails (as opposed to aircraft-affected cirrus) rarely last 9 h. Aircraft-affected cirrus, on the other hand, produce large particles that are affected by sedimentation (e.g., [1,30]). Sedimentation of such aircraft-affected cirrus is accounted for here at the grid scale.

Omitting line-contrail advection should similarly have limited impact in a global model and may in fact reduce numerical diffusion in such a model. For example, even in an extreme case of line-contrail outbreak followed by formation of aircraft-affected cirrus over a period of 17 hours, the maximum area of the aircraft-affected cirrus was 35,000 km<sup>2</sup> [30], smaller than the grid cell area of a  $4 \times 5$  or  $2 \times 2.5$  degree horizontal-resolution model. If a model treats line-contrail advection in such a case by aggregating water from all line contrails into one value in a grid cell then solving advection equations, the water is artificially spread among multiple grid cells when, in fact, the spreading should be limited to the original cell. The present model partly overcomes this problem by isolating line contrails until they have diluted to the grid scale, so individual line contrail water can never numerically diffuse over multiple cells. Only when line contrail material is added to the grid scale can it numerically diffuse. The delay between line contrail formation and transition to cirrus must reduce overall numerical diffusion although it may also cause some error in the location of the line contrails.

In sum, subgrid line contrails form, grow, dilute, and disappear in isolation, and the resulting grid-scale material advects and sediments, helping to form or enhance cirrus in the same or other grid cells. In reality, some contrails persist as cirrus rather than grow from contrail remnants. Nevertheless, the method is an improvement over current parameterizations of contrail-induced cirrus in 3-D models, which do not treat the development or shape of individual line contrails so cannot treat the high relative humidities or the size distribution of aerosols or contrails in individual exhaust plumes.

### 2.13. Relationship to schmidt-appleman criterion

The approach described for determining whether contrails form has some similarities to and differences from the Schmidt–Appleman (S–A) criterion, both in terms of the time scale of its application and the physical nature of the equations.

First, the S–A criterion gives information about contrail formation during the first few seconds after emission but not about contrail persistence since it does not consider plume spreading and twisting due to turbulence and wind shear. The present method calculates formation and dissipation/persistence with time-dependent equations that depend on plume supersaturation and volume a few to tens of seconds after emissions (when plume temperatures have diluted close to ambient temperatures) and plume twisting and spreading over minutes to hours after that due to wind shear and turbulence.

Second, the S–A criterion assumes contrail formation based on water vapor emissions, heat of combustion, and propulsion efficiency of the aircraft as well as air pressure and relative humidity. It ignores, however, information about the size and composition of aerosol particles and assumes contrail formation is time-independent. The present method accounts for aircraft water vapor emissions, the ambient relative humidity, and pressure, as with the S–A criteria, but it does not depend on heat of combustion or propulsion efficiency because the aerosol nucleation and activation equations are assumed to apply upon cooling of the plume to ambient temperature, which occurs a few to tens of seconds after emissions. More important, the present method accounts for the diffusion-limited time-dependent, non-equilibrium transfer of water vapor to aerosol particles of different size and composition (allowing some particles to grow and others to shrink), and for the Kelvin effect and Raoult's law. This helps to determine line contrails persistence and size-dependent optical properties, which the S–A criterion does not do. Results discussed shortly, though, suggest that the present method predicts contrail formation in the same altitude region as the S–A criterion, suggesting that the main factors in determining contrail formation are aircraft water vapor emissions and ambient relative humidity, which are accounted for with both methods.

## 3. Evaluation

Here, the new contrail microphysical algorithms developed are first analyzed in box-model mode against a high-temporal resolution numerical solution for accuracy, stability, and the choice of calculation order. The 3-D model is then evaluated against data with respect to some meteorological, contrail, and aerosol variables.

### 3.1. Comparison of with high-resolution solution

The model is first tested for a single plume against a numerical solution at high temporal resolution. For the simulation, coagulation, nucleation, water vapor deposition/sublimation, and bin partitioning are solved in sequence over one hour with the numerical techniques described. No plume spreading or shearing is treated. Three operator-splitting time steps are used, 1 min, 15 min, and 1 hour. Thus, in the one-hour case, only one time step is taken for each physical process, whereas in the 1-min case, 60 time steps are taken. In all three simulations, the initial size distribution is the same and consists of emitted BC, POM, and S (VI).

Solutions for all time steps are mass-conserving, positive-definite, unconditionally-stable, and non-iterative (Fig. 2(a)). Particles  $<0.1 \mu\text{m}$  diameter, do not nucleate to contrail particles primarily because the Kelvin effects increases vapor pressures over such particles. All time steps predict about the same size distribution of contrail particles  $>2 \mu\text{m}$  diameter. For smaller sizes, accuracy with a 1-h time step diminishes. However, contrail-sized particles are the most optically relevant.

The relative similarity of the contrail mode prediction for all time steps suggests that this scheme can be used at a long time step without significant loss of accuracy in the contrail distribution.

### 3.2. Evaluation of the order of calculation

Next, an additional simulation is run under the same conditions as in Fig. 2(a) to determine the impact of order of calculation on the result in the 1-h time step case. For the new simulation, the order of calculation is nucleation, deposition/sublimation, bin partitioning, coagulation rather than coagulation, nucleation, deposition/sublimation, bin partitioning. Fig. 2(b) indicates that the contrail mode is predicted nearly identically in both cases, but the submicron aerosol mode differs because, when growth is solved first, more particles enter the size range 0.1–1  $\mu\text{m}$  prior to coagulation than when coagulation is solved first, and larger particles coagulate faster than the same number of smaller particles. As such, in the growth  $\rightarrow$  coagulation case, the final aerosol peak is lower and the size distribution is spread more than in the coagulation  $\rightarrow$  growth case. However, because coagulation occurs before growth in an exhaust plume (since growth can occur only when temperatures drop sufficiently in the plume, Section 2.4), the coagulation  $\rightarrow$  growth case should be more physical. Nevertheless, both calculations give nearly identical contrail-mode size distributions, so the order of calculation should not be a significant issue.

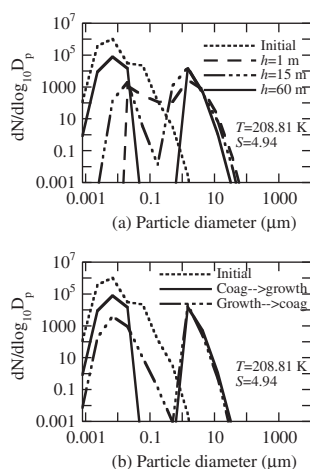
### 3.3. Evaluation of conservation and stability for other conditions

In order to test the conservation and stability properties of the schemes under a variety of other conditions, including during liquid contrail formation, several additional plume-scale tests are run without shearing or spreading. Fig. 3(a)–(f) show the results after a single one-hour time step of coagulation followed by nucleation and condensation/evaporation ( $T > 258.15\text{ K}$ ) or deposition/sublimation ( $T \leq 258.15\text{ K}$ ), and bin partitioning. Results in all cases are mass-conservative, unconditionally stable, and positive-definite.

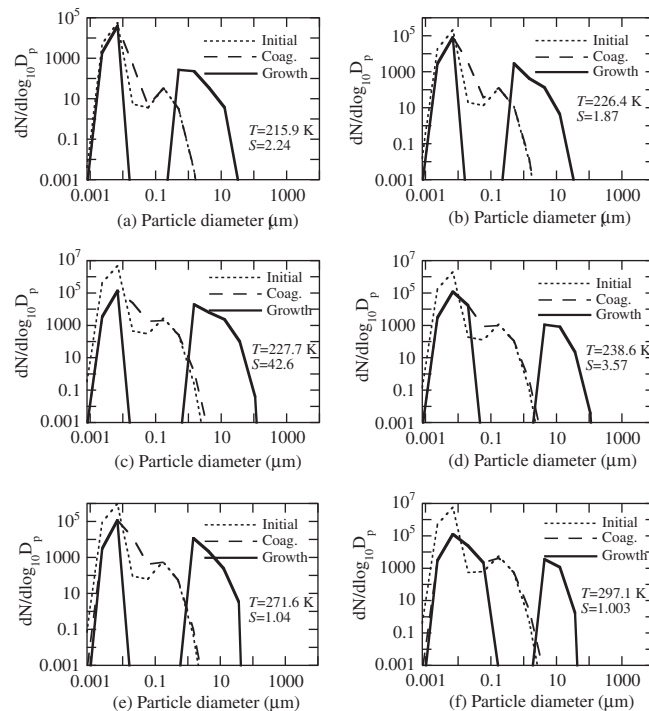
The resulting size distributions are bimodal since the Kelvin effect prevents the smallest particles from growing to contrail-particle size. Contrail particles grow to 0.5–10  $\mu\text{m}$  after one step, well within the observed size range of young line contrail ice crystals [effective diameter  $< 5\text{ }\mu\text{m}$ , [11]. A small tail of particles grows to 50  $\mu\text{m}$ . Results also suggest that coagulation reduces the number concentration of aircraft exhaust particles  $< 20\text{ nm}$  diameter by 1–2 orders of magnitude when the initial number concentration is high.

### 3.4. Comparisons with temperature profile, water vapor profile, and global RH<sub>i</sub> data

The purpose of developing subgrid contrail treatment is to use it in a 3-D model. The 3-D model used here is GATOR-GCMOM, whose previous evaluation is detailed in Jacobson [19]. The processes within the model have also been compared with those in other coupled climate-weather-air pollution models in Zhang [48]. Here, a few additional comparisons with data relevant to contrail formation are provided.



**Fig. 2.** (a) Comparison of plume model microphysical calculations (coagulation, nucleation, water vapor deposition/sublimation, and bin partitioning) at three operator-split time steps (1 min, 15 min, and 1 h). In the one-hour case, one time step is taken for each physical process; in the 1-min case, 60 time steps are taken. The temperature and initial water saturation ratio are given in the figure. The initial size distribution is calculated from aircraft exhaust emitted into an initial contrail plume with the cross-sectional area of a small ellipse, as described in the text. No plume shearing or spreading occurs. (b) Same as (a), but for the 1-h time step case with the order of calculation nucleation, deposition/sublimation, bin partitioning, coagulation instead of the order coagulation, nucleation, deposition/sublimation, bin partitioning.

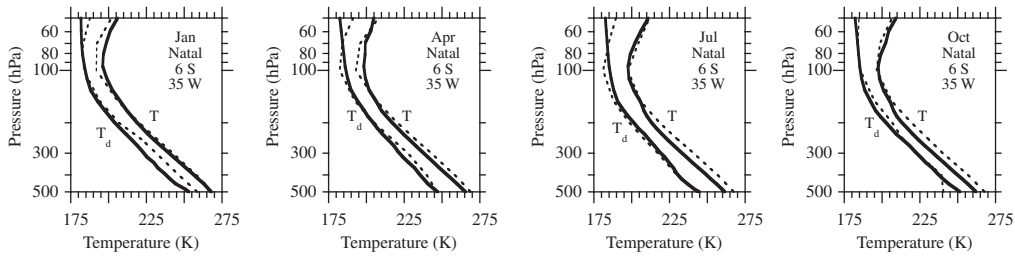


**Fig. 3.** Example calculations of operator-split contrail coagulation (“Coag.”) of an initial size distribution (“Initial”) followed by condensation/evaporation ( $T > 258.15$  K) or deposition/sublimation ( $T \leq 258.15$  K) (“Growth”) onto the coagulated distribution, then bin partitioning over a single one-hour time step, given the temperature and initial water saturation ratio in the figure. Other conditions are the same as in Fig. 2(a).

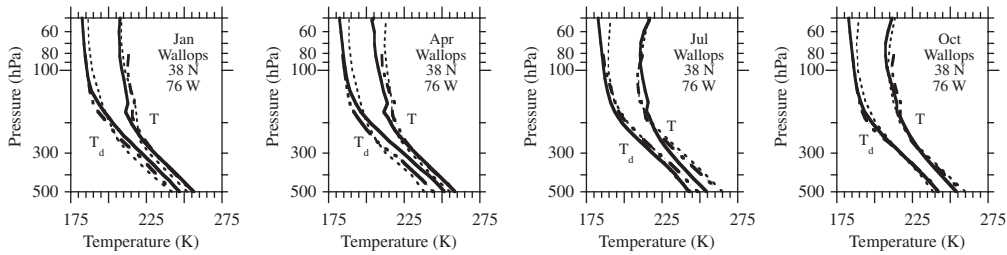
For the simulations the horizontal resolution over the global domain is  $4^\circ \text{ S-N} \times 5^\circ \text{ W-E}$  and that over a one-way nested US domain is  $0.5^\circ \text{ S-N} \times 0.75^\circ \text{ W-E}$  ( $\sim 55 \text{ km S-N} \times 68 \text{ km W-E}$ ). For the first set of simulations, the global domain is set to 51 sigma-pressure layers up to 0.219 hPa ( $\approx 60 \text{ km}$ ), with 500-m vertical resolution from 1–13 km, 1 km resolution from 13–21 km, and eight layers in the bottom kilometer. Since all flights occur at or below 41,000 ft (12.5 km), the 500-m resolution up to 13 km only is sufficient. The nested U.S. domain includes 35 layers matching these global layers up to 75.6 hPa ( $\approx 18 \text{ km}$ ). The model is initialized for this case with  $1^\circ \times 1^\circ$  global reanalysis fields for 12 GMT January 1, 2004 [10] and uses 2004 aircraft emissions [46]. For nested simulations, emissions occur in both domains, but the regional domain uses global-domain information for meteorological and chemical inflow at the horizontal boundaries [14] and ozone predicted above the regional model top for radiation calculations. Operator-split time intervals for contrail processes are 30 min for the regional domain and 1 h for the global domain. The computer time of the model with the subgrid treatment of 31 million flights annually on the global domain is about 20–25% greater than with no treatment of aircraft exhaust (e.g., 10.4 days/year of simulation without aircraft for  $4 \times 5^\circ$  horizontal resolution and 51 vertical layers and an additional 2.1–2.5 days/year with aircraft on 16 Xeon Nehalem 5580, 3.2 GHz compute cores).

Fig. 4 compares baseline modeled vertical profiles of temperature and dew point with monthly 2004 sounding data at the exact locations (paired-in-space) of the data for (a) the global domain and (b) the US regional domain of the nested global-US simulation. Temperature ( $T$ ) gives saturation vapor pressure over liquid and ice and dew point ( $T_d$ ) gives partial pressure of water vapor. RH alone is not compared directly with data because the instrument used for most  $T$  and  $T_d$  measurements in 2004 was the Vaisala RS80–56H, which the manufacturer estimates has  $\sim 0.5$  K total uncertainty in temperature. Miloshevich et al. [29] referenced a dry bias in the RS80–56H instrument of 4% of the measured RH at 233 K, 13% at 213 K, and 32% at 193 K. However, these combined errors in RH and  $T$  translate into  $T_d$  errors of only  $\sim 0.9$  K at 233 K,  $\sim 1.6$  K at 213 K, and  $\sim 2.7$  K at 193 K under high RH conditions and lesser errors under low RH conditions. These errors would not significantly affect the comparisons in Fig. 4, as air temperatures are only seasonally  $< 213.15$  K.

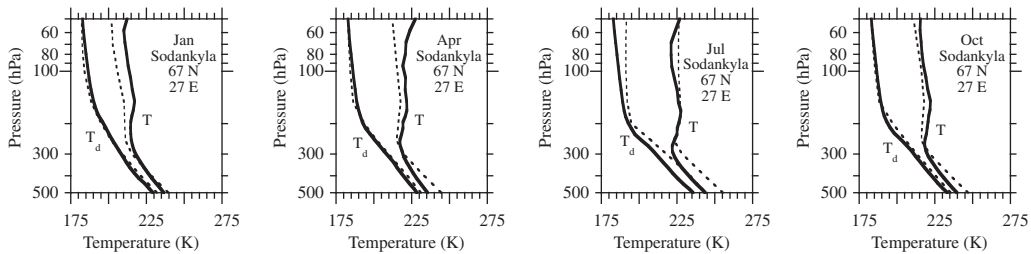
The results in Fig. 4, obtained without model spinup or data assimilation (the model is entirely prognostic), indicate general agreement for the global domain considering its coarse  $4 \times 5^\circ$  resolution, particularly at pressures of most contrail formation (150–350 hPa). For example, the modeled October temperature and dew point profiles at Natal (6 S), Wallops (38 N), Sodankyla (67 N), and Ny Alesund (79 N) are nearly on top of the measured profiles in this altitude range. An error in dew point of 10 K occurs at 500 hPa at Wallops in April, of 12 K in temperature at Ny Alesund in July at 500 hPa, and of  $> 15$  K at 50 hPa at Ny Alesund in April, but lesser errors occur at other altitudes and seasons. Also, for Wallops (Fig. 4(b)), many global-simulation errors diminish at higher resolution over the US although some errors in dew point of up to 8 K persist.

**(a)**  
Natal

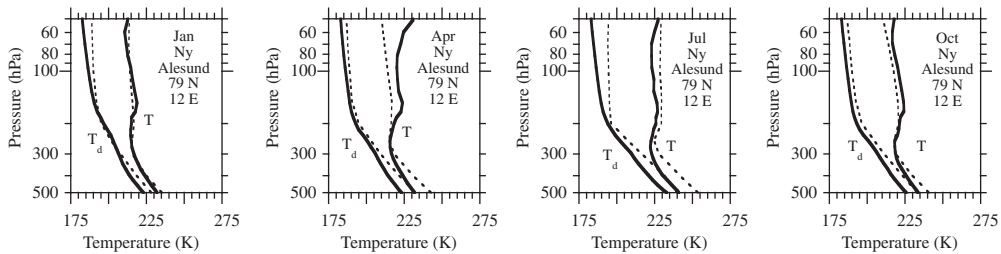
## Wallops Island



## Sodankylä



## Ny Alesund

**(b)**

## Miami, Florida

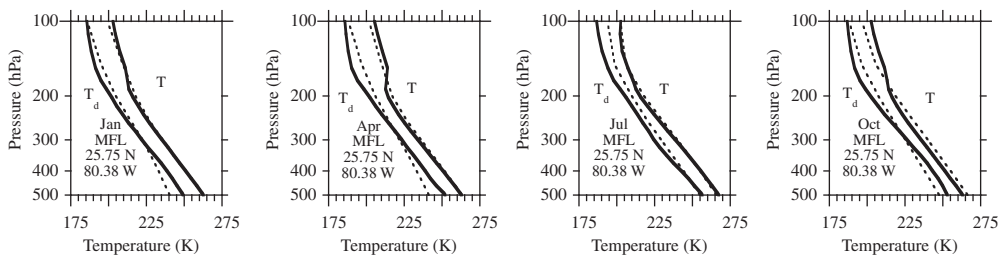


**Fig. 4.** (a) Comparison of monthly-averaged vertical profiles of 2004 global-domain modeled (at  $4^\circ \times 5^\circ$  resolution) (solid lines) and 2004 radiosonde temperature and dew point data [9] (dashed lines) at different locations for January, April, July, and October. For Wallops, model results from the US domain of a nested global-US simulation are shown as well (dash-dot line) (b) Same as (a), but from the US domain of a nested global-US simulation over Miami. The uncertainty in the temperature is  $\sim 0.5$  K and that in the dew point is  $\sim 0.9$  K at 233 K,  $\sim 1.6$  K at 213 K, and  $\sim 2.7$  K at 193 K (see text). The model run is without data assimilation or model spinup.



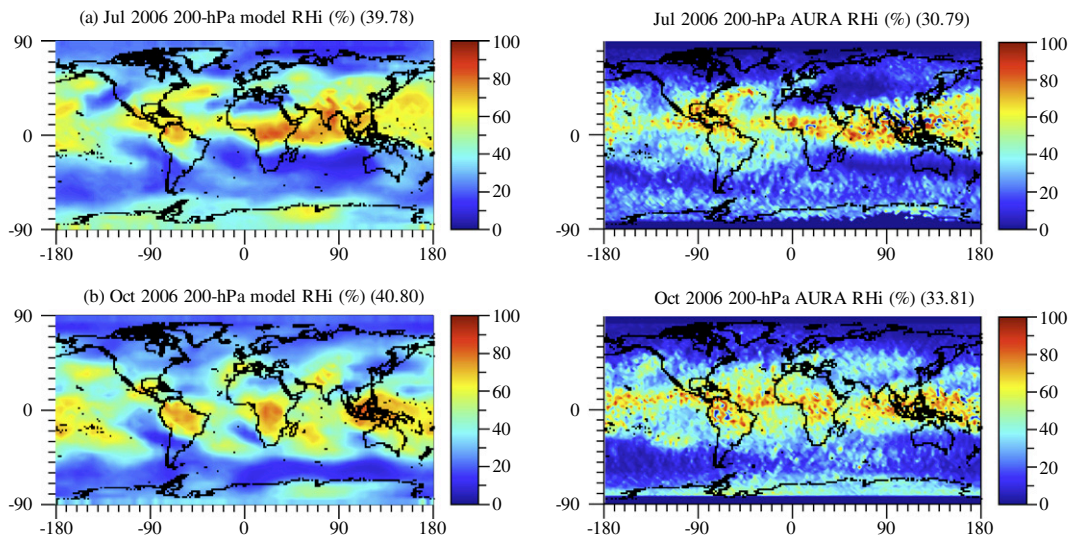


**Fig. 5.** Comparison of modeled with satellite-derived 200-hPa relative humidity over ice (RHi), obtained from the Aura Microwave Limb Sounder (MLS) [33].

In situ  $T_d$  data are thought to be more accurate than satellite-derived supersaturation or relative humidity measurements due to the better spatial resolution and accuracy of in situ data [23]. Nevertheless, a comparison of modeled with satellite relative humidity over ice (RHi) at the height of contrail formation is instructive for determining whether modeled patterns of RHi can be seen in the data and whether supersaturations needed for contrail formation are in the ballpark. Fig. 5 compares modeled with AURA satellite RHi for July and October 2006. Despite the different resolutions ( $4 \times 5^\circ$  for the model;  $2 \times 2.5^\circ$  for the satellite product) and the uncertainties in the model and satellite product, the relative similarities in patterns and magnitudes of several peaks (e.g., mid-Atlantic and mid-Pacific peaks at northern midlatitudes; July and October peaks over equatorial land worldwide; July and October peaks over the Gulf of Mexico) give confidence in predicted contrail cloud fractions, discussed shortly.

### 3.5. Comparison of black carbon vertical profiles with data

The comparisons in Fig. 4 indicate that the model vertical transport and diffusion schemes are not numerically diffusive relative to the data with respect to water vapor. A diffusive scheme would give a closer-to-isothermal dewpoint relative to the data whereas a nondiffusive scheme would give results that either match or are less isothermal than the data. In almost all cases, the modeled dewpoint is either close to matching or less isothermal than the data. GATOR-GCMOM has similarly been shown to be non-diffusive with respect to tropospheric-stratospheric transport of ozone [18]. The limited model vertical numerical diffusion is illustrated further in Fig. 6(a), which compares modeled black carbon vertical profiles with

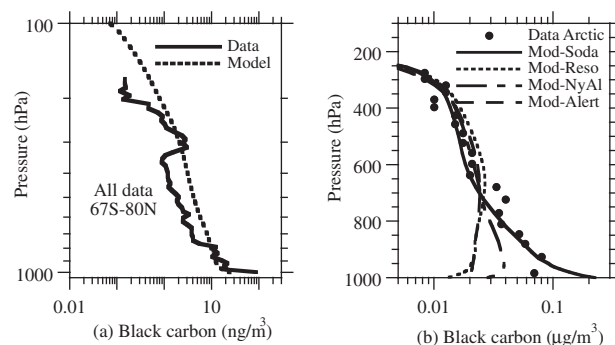


**Fig. 6.** (a) Comparison of GATOR-GCMOM modeled black carbon vertical profiles with data between 67S and 80 N over the Pacific from January 1–31, 2009 from the HIPPO campaign [41]. The model is run at  $4 \times 5^\circ$  resolution. Model and data column loadings are 67 and  $68 \mu\text{g}/\text{m}^2$ , respectively, a 1.4% difference. (b) Comparison of a modified measured vertical profile of black carbon over the Arctic with simulation-averaged March profiles at Sodankylä, Finland (Soda – 67.37 N, 26.65 E), Resolute Bay (Reso – 74.73 N, 94.93 W), Ny Alesund, Norway (NyAl – 78.92 N, 11.93 E), and Alert, Canada (Alert – 82.50 N, 62.33 W). The data profile is obtained as described in the text.



data between 67S and 80 N over the Pacific from January 1–31, 2009 from the HIPPO campaign [41]. This simulation uses 68 layers from 0–60 km. Model and data column loadings are 67 and  $68 \mu\text{g}/\text{m}^2$ , respectively, a 1.4% difference, and the slope of the mean modeled vertical profile is similar to that of the data, indicating little model vertical numerical diffusion. This relative accuracy contrasts with results from a set of 14 other global models tested against the same data by Schwarz et al. [41], who concluded that such models “over-predicted BC concentrations overall by a factor of five” and found modeled vertical profile slopes effectively vertical in the troposphere, an indicator of numerical diffusion.

Fig. 6(b) compares the vertical profiles of modeled BC (with 51 layers from 0–60 km), averaged over all months of March at several Arctic locations with data from March 1983 aircraft measurements, reported in Hansen and Novakov [12] over Alaska, Canada, and Greenland, extrapolated in time to the early 2000s using the surface trend at Alert given in Quinn et al. [38]. The Quinn et al. data suggest a significant decrease in BC from 1990–1999, but then a leveling off. Their data are first extrapolated linearly backward to 1983 (since their data were not available prior to 1990), then their 1999:1983 concentration ratio (1/6) are used to scale the vertical profile measurements from 1983 to 1999, and this profile is assumed to hold for subsequent years. Fig. 6(b) shows that, between 250–700 hPa, the modeled BC profiles at all locations line up extremely well with the extrapolated measured profile. At altitudes below 700 hPa, the modeled profiles near Europe (Sodankyla, Ny Alesund) match the measured profile better than those over more remote locations (Resolute, Alert). These results, along with those of Fig. 6(a), indicate that the model is probably not overpredicting BC in the vertical profile.

### 3.6. Modeled contrail cloud fraction versus data over the US

A Global-US nested simulation is run to evaluate 3-D predictions of contrail coverage with the subgrid aircraft treatment described here. Fig. 7 compares January modeled contrail cloud fraction from the US with satellite-inferred data [7]. The modeled values are 24-h averages over a month and account for all line contrails whereas the data are from two overpasses per day for a month (a daytime overpass from MODIS on the Terra satellite and a nighttime overpass for MODIS on the Aqua satellite). Also the data cover irregularly-shaped regions and account for line contrails with optical depths only  $>\sim 0.02$  (e.g., [35,27]). Nevertheless, the comparisons reveal significant similarities. The domain-averaged modeled contrail cloud fraction (0.0062) is within 9% of the observed averages (0.0068), and many locations of observed high or low contrail cloud fraction are modeled in both months (e.g., northeast US, eastern seaboard, upper Midwest). Differences occur in the southwest US and southern Pacific.

### 3.7. Modeled global contrail cloud fraction

A global simulation using 2006 emissions is used to evaluate global contrail cloud fraction and other contrail properties. The simulation results in a time- and globally-averaged linear contrail cloud fraction (with no optical depth threshold) of 0.0014 (Fig. 8). This compares with Ponater et al. [35]’s modeled values for all contrails (no optical depth threshold) of

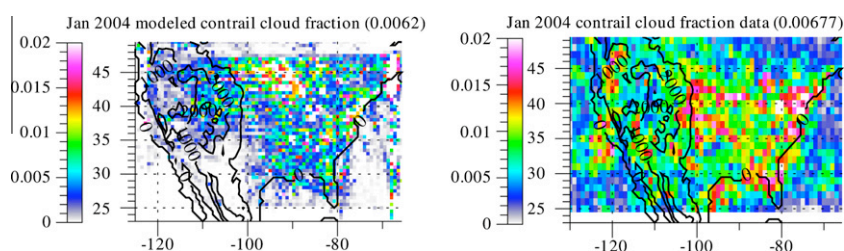


**Fig. 7.** Modeled US domain ( $0.5^\circ \times 0.75^\circ$  resolution) versus observed [7] January 2004 contrail cloud fraction. Modeled values are 24-h averages over a month whereas the data are from two instantaneous overpasses per day for a month. Numbers in parenthesis are domain averages.

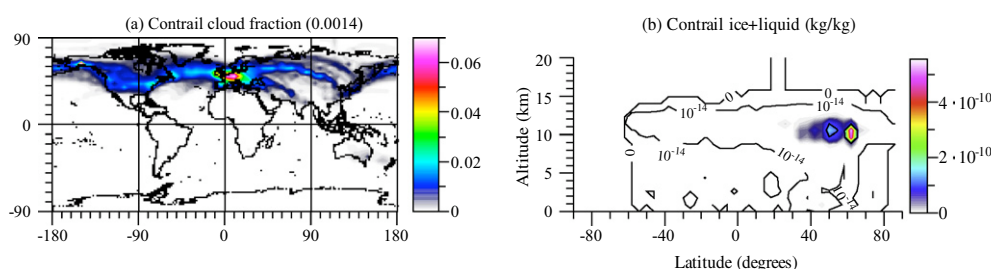


**Fig. 8.** Annual-averaged modeled (a) global contrail cloud fraction, (b) zonally-averaged contrail water from simulations using 2006 aircraft emissions.

0.0014 using early 1990s aircraft emissions and Burkhardt and Kärcher [3]'s modeled contrail cloud fraction of 0.0010 with Aero2K emissions. It also compares with 2015 modeled values (with a 0.02 optical depth threshold) of 0.0014 from Marquart et al. [27]. Thus, the estimated global contrail coverage here is well within the extrapolated range of other model estimates and their uncertainty for 2006 emissions.

Most modeled contrails form from 30–65°N (Fig. 8). Whereas, modeled line contrails form only near aircraft emissions [a map of which is shown in [46]], aircraft emissions do not always lead to contrails. Contrails form primarily in the US and Europe but less readily in southeast East Asia, consistent with data. Meyer et al. [28] derived annual contrail cloud fractions from satellite in Japan and Thailand of 0.0025 and 0.0013, respectively, for 1998. The modeled values in Fig. 8 in those locations are  $\sim 0.004$  and  $0.0015$ , respectively.

Aircraft emissions (at the subgrid scale) peak vertically between 10.5–11.5 km (246–211 hPa) above sea level [46]. The increase in aircraft water vapor and particles at these heights causes subgrid contrails to form there (Fig. 8). The height range of most modeled contrails away from the poles is well within the height range of non-polar contrail formation determined from the Schmidt–Appleman criterion, 8.4–14 km [40]. Some liquid contrail particles form at airports in the presence of high relative humidities there. These contrails are analogous to condensation from the exhaust of an automobile that occurs during a cold morning.

### 3.8. Modeled contrail widths, spreading times, and optical depths

From the global simulation, the modeled annual mean line contrail width between formation and disappearance (upon a reduction in water content to  $<10 \mu\text{g}/\text{m}^3$ ) is  $\sim 2.5$  km. Line contrail disappearance occurs predominantly when widths are  $<5$  km, occasionally 5–10 km, and rarely 10–15 km, all much smaller than the width of a global ( $\sim 440$  km) or regional ( $\sim 60$  km) domain grid cell in the present model setup.

Table 3 provides typical times required for spreading of the top-view area of the elliptical cross section of a contrail plume as calculated by the subgrid plume module, for some conditions of turbulence and shear. The most relevant conditions are those with low or medium shear, as the no-shear cases are highly improbable. Under shear conditions, the time required for contrail top-view cross-sectional spreading to 5 km ranges from 1–3.4 h; that required for spreading to 10 km is 1.5–6.7 h. For comparison, Duda et al. [5] observed contrail widths from satellite over the Great Lakes of 8 km after 2 h. Some widths of 10 km were also observed. Minnis et al. [30] observed the evolution of contrails to contrail-induced cirrus over periods ranging from 7 to 17 h, but the distinction between line contrails and contrail-induced cirrus was difficult to discern after 2–4 h in all cases.

Contrail optical depths vary with time between formation and dissipation. Since the optical depth depends on the snapshot in time when the optical depth value is considered, there is no unique optical depth that characterizes contrails. For optical depths  $>0.01$ , average contrail optical depths here generally vary from 0.06–0.15, similar to 0.1–0.3 from Stuber and Forster [43].

## 4. Summary

This paper provides and evaluates numerical techniques for simulating the evolution of discrete, size- and composition-resolved aerosol and contrail particles in individual aircraft exhaust plumes in a global or regional 3-D atmospheric model and the coupling of the subgrid exhaust plume information to the grid scale. Such treatment represents a new method of simulating the effects of aircraft on climate, contrails, and atmospheric composition. Microphysical processes within each plume include size-resolved coagulation among and between aerosol and contrail particles and their inclusions, aerosol-to-hydrometeor particle ice nucleation, condensation/evaporation, and deposition/sublimation.

Size-resolved contrail-particle core composition is tracked throughout the evolution of each plume. Each subgrid exhaust plume in a grid cell is unique in that it has its own emissions and supersaturation (which is a function of ambient and emitted water vapor). When line contrails sublimate/evaporate, their aerosol cores and water vapor are added to the grid scale, where they affect grid-scale externally- and internally mixed aerosol particles, stratus clouds, and subgrid cumulus clouds. Cloud fraction is determined by accounting for the shape of each line contrail and random overlap among line

**Table 3**

Time required for contrails to spread 5, 10, or 15 km for given constant turbulence and shear levels in the subgrid plume module.

	5 km	10 km	15 km
Low turbulence ( $D_h = 5, D_v = 0 \text{ m}^2/\text{s}$ ), no shear	7 d	29 d	65 d
Med. turbulence ( $D_h = 10, D_v = 0.1 \text{ m}^2/\text{s}$ ), no shear	3.5 d	14.5 d	32.5 d
High turbulence ( $D_h = 20, D_v = 0.5 \text{ m}^2/\text{s}$ ), no shear	1.8 d	7 d	16 d
Med. turb. ( $D_h = 10, D_v = 0.1 \text{ m}^2/\text{s}$ ), low shear (0.001/s)	3.4 h	6.7 h	10 h
High turb. ( $D_h = 20, D_v = 0.5 \text{ m}^2/\text{s}$ ), med. shear (0.005/s)	1 h	1.5 h	2.5 h

$D_h$  and  $D_v$  are horizontal and vertical diffusion coefficients, respectively; h is hours; d is days.

contrails, subgrid cumulus clouds, and grid-scale stratiform clouds. Cloud optical properties account for absorbing inclusions in all cloud particles of each size, including contrail, cumulus, and stratus (liquid, ice, and graupel).

Evaluation of the schemes, all of which are non-iterative, indicate they are mass conserving, positive-definite, and unconditionally-stable. Application of the schemes in a 3-D model indicates the overall model with the treatment of subgrid contrails can simulate observed relative humidity over ice and contrail cloud fraction to the correct order and with reasonable spatial distribution. Further tests against observations indicate that the 3-D model results in little vertical numerical diffusion of water vapor or black carbon transport. Finally, the computer time of the overall GATOR-GCMOM model with the subgrid treatment of 31 million flights annually is about 20–25% greater than with no treatment of aircraft. As such, the method described can be used for global and regional-scale studies.

## Acknowledgments

This work was supported by the Partnership for Air Transportation Noise & Emissions Reduction (PARTNER) and the Federal Aviation Administration (FAA) under award DTFAWA-05-D-0006. Any opinions, findings, and conclusions or recommendations expressed are those of the authors and do not necessarily reflect the views of PARTNER or the FAA. We thank Daniel Whitt for preparing Aura data.

## References

- [1] D. Atlas, Z. Wand, D.P. Duda, Contrails to cirrus – morphology, microphysics, and radiative properties, *J. Appl. Meteorol. Clim.* 45 (2006) 5–19.
- [2] K.V. Beard, H.T. Ochs III, Collection and coalescence efficiencies for accretion, *J. Geophys. Res.* 89 (1984) 7165–7169.
- [3] U. Burkhardt, B. Kärcher, Process-based simulation of contrail cirrus in a global climate model, *J. Geophys. Res.* 114 (2009) D16201, doi:10.1029/2008JD011491.
- [4] P.J. DeMott, An exploratory study of ice nucleation by soot aerosols, *J. Appl. Meteorol.* 29 (1990) 1072–1079.
- [5] D.P. Duda, P. Minnis, L. Nguyen, R. Palikonda, A case study of the development of contrail clusters over the great lakes, *J. Atmos. Sci.* 61 (2004) 1132–1146.
- [6] D.P. Duda, P. Minnis, R. Palikonda, Estimated contrail frequency and coverage over the contiguous United States from numerical weather prediction analyses and flight track data, *Meteorologica Zeitschrift* 14 (2005) 537–548.
- [7] D.P. Duda, R. Palikonda, P. Minnis, Relating satellite and surface detection of contrails to numerical weather output, *Atmos. Chem. Phys.* 9 (2009) 1357–1364.
- [8] M.C. Facchini, M. Mircea, S. Fuzzi, R.J. Charlson, Cloud albedo enhancement by surface-active organic solutes in growing droplets, *Nature* 401 (1999) 257–259.
- [9] Forecast Systems Laboratory (FSL) (2008) Recent worldwide RAOB observations CDROM, <<http://www.fsl.noaa.gov/data/onlinebd.html>>.
- [10] Global Forecast System (GFS) (2007)  $1^\circ \times 1^\circ$  reanalysis fields, <<http://nomads.nccdc.noaa.gov/data/gfs-avn-hi/>>.
- [11] J. Goodman, R.F. Pueschel, E.J. Jensen, S. Verma, G.V. Ferry, S.D. Howard, S.A. Kinne, D. Baumgardner, Shape and size of contrails ice particles, *Geophys. Res. Lett.* 25 (9) (1998) 1327–1330, doi:10.1029/97GL03091.
- [12] A.D.A. Hansen, T. Novakov, Aerosol black carbon measurements in the Arctic haze during AGASP II, *J. Atmos. Chem.* 9 (1989) 347–361.
- [13] E.E. Hindman II, D.B. Johnson, Numerical simulation of ice particle growth in a cloud of supercooled water droplets, *J. Atmos. Sci.* 29 (1972) 1313–1321.
- [14] M.Z. Jacobson, GATOR-GCMM: a global through urban scale air pollution and weather forecast model. 1. Model design and treatment of subgrid soil, vegetation, roads, rooftops, water, sea ice, and snow, *J. Geophys. Res.* 106 (2001) 5385–5402.
- [15] M.Z. Jacobson, Analysis of aerosol interactions with numerical techniques for solving coagulation, nucleation, condensation, dissolution, and reversible chemistry among multiple size distributions, *J. Geophys. Res.* 107 (D19) (2002) 4366, doi:10.1029/2001JD002044.
- [16] M.Z. Jacobson, Development of mixed-phase clouds from multiple aerosol size distributions and the effect of the clouds on aerosol removal, *J. Geophys. Res.* 108 (D8) (2003) 4245, doi:10.1029/2002JD002691.
- [17] M.Z. Jacobson, *Fundamentals of Atmospheric Modeling*, second ed., Cambridge University Press, New York, 2005. pp. 813.
- [18] M.Z. Jacobson, Effects of wind-powered hydrogen fuel cell vehicles on stratospheric ozone and global climate, *Geophys. Res. Lett.* 35 (2008) L19803, doi:10.1029/2008GL035102.
- [19] M.Z. Jacobson, Short-term effects of controlling fossil-fuel soot, biofuel soot and gases, and methane on climate, Arctic ice, and air pollution health, *J. Geophys. Res.* 115 (2010) D14209, doi:10.1029/2009JD013795.
- [20] M.Z. Jacobson, D.B. Kittelson, W.F. Watts, Enhanced coagulation due to evaporation and its effect on nanoparticle evolution, *Environ. Sci. Technol.* 39 (2005) 9485–9492.
- [21] M.Z. Jacobson, Y.J. Kaufmann, Y. Rudich, Examining feedbacks of aerosols to urban climate with a model that treats 3-D clouds with aerosol inclusions, *J. Geophys. Res.* 112 (2007) D24205, doi:10.1029/2007JD008922.
- [22] Z.A. Kanji, J.P.D. Abbatt, Laboratory studies of ice formation via deposition mode nucleation onto mineral dust and *n*-hexane soot samples, *J. Geophys. Res.* 111 (2006) D16204, doi:10.1029/2005JD006766.
- [23] N. Lamquin, C.J. Stubenrauch, J. Pelon, Upper tropospheric humidity and cirrus geometrical and optical thickness: relationships inferred from 1 year of collocated AIRS and CALIPSO data, *J. Geophys. Res.* 113 (2008) D00A08, doi:10.1029/2008JD010012.
- [24] J. Liang, M.Z. Jacobson, Effects of subgrid mixing on ozone production in a chemical model, *Atmos. Environ.* 34 (2000) 2975–2982.
- [25] R.F. Lin, D.O. Starr, P.J. DeMott, W. Cotton, K. Sassen, E. Jensen, B. Kärcher, X. Liu, Cirrus parcel model comparison project, phase 1: the critical components to simulate cirrus initiation explicitly, *J. Atmos. Sci.* 59 (2002) 2305–2329.
- [26] T.B. Low, R. List, Collision, coalescence and breakup of raindrops. Part I: experimentally established coalescence efficiencies and fragment size distributions in breakup, *J. Atmos. Sci.* 39 (1982) 1591–1606.
- [27] S. Marquart, M. Ponater, F.R. Mager, R. Sausen, Future development of contrail cover, optical depth, and radiative forcing: impacts of increasing air traffic and climate change, *J. Clim.* 16 (2003) 2890–2904.
- [28] R. Meyer, R. Buell, C. Leiter, H. Mannstein, S. Pechtl, T. Oki, P. Wendling, Contrail observations over Southern and Eastern Asia in NOAA/AVHRR data and comparisons to contrail simulations in a GCM, *Int. J. Remote Sens.* 28 (2007) 2049–2069.
- [29] L.M. Miloshevich, H. Vomel, D.N. Whiteman, B.M. Lesht, F.J. Schmidlin, F. Russo, Absolute accuracy of water vapor measurements from six operational radiosonde types launched during AWEX-G and implications for AIRS validation, *J. Geophys. Res.* 111 (2006) D09S10, doi:10.1029/2005JD006083.
- [30] P. Minnis, D.F. Young, D.P. Garber, L. Nguyen, W.I. Smith Jr., R. Palikonda, Transformation of contrails into cirrus during SUCCESS, *Geophys. Res. Lett.* 25 (1998) 1157–1160.
- [31] O. Mohler et al., Effect of sulfuric acid coating on heterogeneous ice nucleation by soot aerosol particles, *J. Geophys. Res.* 110 (2005) D11210, doi:10.1029/2004JD005169.
- [32] A.D. Naiman, S.K. Lele, J.T. Wilkerson, M.Z. Jacobson, Parameterization of subgrid plume dilution for use in large-scale atmospheric simulations, *Atmos. Chem. Phys.* 10 (2010) 2551–2560.

- [33] National Aeronautics and Space Administration (NASA) (2010) EOS Aura Data Support Web Site, <<http://disc.sci.gsfc.nasa.gov/Aura>>.
- [34] A. Petzold, A. Doppelheuer, C. Brock, F. Schroder, In situ observations and model calculations of black carbon emission by aircraft at cruise altitude, *J. Geophys. Res.* 104 (1999) 22,171–22,181.
- [35] M. Ponater, S. Marquart, R. Sausen, Contrails in a comprehensive global climate model: parameterization and radiative forcing results, *J. Geophys. Res.* 107 (2002) 4164, doi:[10.1029/2001JD000429](https://doi.org/10.1029/2001JD000429).
- [36] H.R. Pruppacher, J.D. Klett, *Microphysics of Clouds and Precipitation*, 2nd rev. and enl. ed., Kluwer Academic Publishers, Dordrecht, 1997.
- [37] A. Rap, P.M. Forster, A. Jones, O. Boucher, J.M. Haywood, N. Bellouin, R.R. De Leon, Parameterization of contrails in the UK Met Office climate model, *J. Geophys. Res.* 115 (2010) D10205, doi:[10.1029/2009JD012443](https://doi.org/10.1029/2009JD012443).
- [38] P.K. Quinn, G. Shaw, E. Andres, E.G. Dutton, T. Ruoho-Airola, S.L. Gong, Arctic haze: current trends and knowledge gaps, *Tellus B* 59 (2007) 99–114.
- [39] D. Rind, P. Lonergan, K. Shah, Modeled impact of cirrus cloud increases along aircraft flight paths, *J. Geophys. Res.* 105 (2000) 19,927–19,940.
- [40] U. Schumann, On conditions for contrail formation from aircraft exhausts, *Meteorol. Zeitschrift* 5 (1996) 4–23.
- [41] J.P. Schwarz, J.R. Spackman, R.S. Gao, L.A. Watts, P. Stier, M. Schulz, S.M. Davis, S.C. Wofsy, D.W. Fahey, Global-scale black carbon profiles observed in the remote atmosphere and compared to models, *Geophys. Res. Lett.* 37 (2010) L18812, doi:[10.1029/2010GL044372](https://doi.org/10.1029/2010GL044372).
- [42] C. Snow, Formulas for computing capacitance and inductance, *Natl. Bur. Stand. Circ.* 544, Washington, D.C., U.S. Dept. of Commerce, 69, 1954.
- [43] N. Stuber, P. Forster, The impact of diurnal variations of air traffic on contrail radiative forcing, *Atmos. Chem. Phys.* 7 (2007) 3153–3162.
- [44] P.F. Vohralik, L.K. Randeniya, I.C. Plumb, S.L. Baughcum, Effect of plume processes on aircraft exhaust, *J. Geophys. Res.* 113 (2008) D05312, doi:[10.1029/2007JD008982](https://doi.org/10.1029/2007JD008982).
- [45] P.D. Whitefield et al., Summarizing and interpreting aircraft gaseous and particulate emissions data, Aircraft Cooperative Research Program, Report 9, Transportation Research Board, Washington, D.C., 2008.
- [46] J.T. Wilkerson, M.Z. Jacobson, A. Malwitz, S. Balasubramanian, R. Wayson, G. Fleming, A.D. Naiman, S.K. Lele, Analysis of emission data from global commercial aviation: 2004 and 2006, *Atmos. Chem. Phys.* 10 (2010) 6391–6408.
- [47] P.M. Winkler, A. Vrtala, R. Rudolf, P.E. Wagner, I. Riipinen, T. Vesala, K.E.J. Lehtinen, Y. Viisanen, M. Kulmala, Condensation of water vapor: experimental determination of mass and thermal accommodation coefficients, *J. Geophys. Res.* 111 (2006) D19202, doi:[10.1029/2006JD007194](https://doi.org/10.1029/2006JD007194).
- [48] Y. Zhang, Online-coupled meteorological and chemistry models: history, current status, and outlook, *Atmos. Chem. Phys.* 8 (2008) 2895–2932.
- [49] Y. Zhu, W.C. Hinds, S. Kim, S. Sioutas, Concentration and size distribution of ultrafine particles near a major highway, *J. Air Waste Manage. Assoc.* 52 (2002) 1032–1042.